

Geophysical Research Letters

RESEARCH LETTER

10.1029/2020GL087607

Key Points:

- Ringwoodite thermal conductivity is reduced by 40% due to the presence of 1.73 wt% water in the crystal structure
- Lower thermal conductivity of hydrous ringwoodite might delay the breakdown of hydrous phases hosted in a subducting slab
- Hydrous ringwoodite acts as a heat propagation barrier, supporting preservation of hydrous minerals down to the lower mantle

Supporting Information:

- Supporting Information S1

Correspondence to:

E. Marzotto, W.-P. Hsieh, and E. Ohtani,
enrico.marzotto@uni-bayreuth.de;
wphsieh@earth.sinica.edu.tw;
ohtani@m.tohoku.ac.jp

Citation:






Marzotto, E., Hsieh, W.-P., Ishii, T., Chao, K.-H., Golabek, G. J., Thielmann, M., & Ohtani, E. (2020). Effect of water on lattice thermal conductivity of ringwoodite and its implications for the thermal evolution of descending slabs. *Geophysical Research Letters*, 47, e2020GL087607. <https://doi.org/10.1029/2020GL087607>

Received 21 FEB 2020

Accepted 17 MAY 2020

Accepted article online 24 MAY 2020

Effect of Water on Lattice Thermal Conductivity of Ringwoodite and Its Implications for the Thermal Evolution of Descending Slabs

Enrico Marzotto¹ , Wen-Pin Hsieh^{2,3} , Takayuki Ishii¹ , Keng-Hsien Chao², Gregor J. Golabek¹, Marcel Thielmann¹ , and Eiji Ohtani⁴ 

¹Bayerisches Geoinstitut, Universität Bayreuth, Bayreuth, Germany, ²Institute of Earth Sciences, Academia Sinica, Taipei, Taiwan, ³Department of Geosciences, National Taiwan University, Taipei, Taiwan, ⁴Graduate School of Science, Tohoku University, Sendai, Japan

Abstract The presence of water in minerals generally alters their physical properties. Ringwoodite is the most abundant phase in the lowermost mantle transition zone and can host up to 1.5–2 wt% water. We studied high-pressure lattice thermal conductivity of dry and hydrous ringwoodite by combining diamond-anvil cell experiments with ultrafast optics. The incorporation of 1.73 wt% water substantially reduces the ringwoodite thermal conductivity by more than 40% at mantle transition zone pressures. We further parameterized the ringwoodite thermal conductivity as a function of pressure and water content to explore the large-scale consequences of a reduced thermal conductivity on a slab's thermal evolution. Using a simple 1-D heat diffusion model, we showed that the presence of hydrous ringwoodite in the slab significantly delays decomposition of dense hydrous magnesium silicates, enabling them to reach the lower mantle. Our results impact the potential route and balance of water cycle in the lower mantle.

Plain Language Summary The physical properties of minerals are determined by the interaction of atoms in the crystal lattice. Water can be incorporated into the crystal structure and alter its behavior. Ringwoodite is a high-pressure mineral that can host large quantities of water and is expected to be abundant in the lower part of Earth's mantle transition zone, a region ranging from 520 to 660-km depth. Here we studied ringwoodite thermal conductivity, describing how effectively heat is transported through solids. Based on our measurements we determined that water in ringwoodite significantly slows down heat propagation. We performed computer simulations to investigate the large-scale implications of our findings. For this purpose, we modeled a cold oceanic plate, entirely made of ringwoodite, which is surrounded by warm mantle. The delayed heat transport is sufficient to maintain low temperatures in the inner part of the oceanic plate and potentially preserve the hydrous minerals for an extended period of time.

1. Introduction

Ringwoodite is the high-pressure polymorph of olivine that is stable in the lowermost part of the mantle transition zone (MTZ) between approximately 520- to 660-km depth (Suzuki et al., 2000). It is thought that ringwoodite constitutes ≈ 60 vol% of the ambient MTZ (Frost, 2008), and ≈ 80 vol% of the harzburgitic slab (Irfune & Ringwood, 1987). Its abundance, combined with its water solubility of up to 1.5–2 wt% (Inoue et al., 2010; Kohlstedt et al., 1996; Ohtani et al., 2000), makes ringwoodite a potential water reservoir in the MTZ. The presence of water in the Earth's interior affects physical and chemical properties of minerals as well as the solid-state rheology of the convecting mantle (Karato & Jung, 1998; Mei & Kohlstedt, 2000). Natural samples (Pearson et al., 2014; Tschauner et al., 2018) and geophysical observations (Khan & Shankland, 2012; Utada et al., 2009) both suggest that water is probably heterogeneously distributed within the MTZ.

Water can be transported into the Earth's interior through subduction of hydrated oceanic lithosphere (Faccenda, 2014). During subduction, the increase of pressure and temperature with depth results in the breakdown of hydrous phases (Schmidt & Poli, 1998) and the dehydration melting of the mantle wedge (Rüpke et al., 2004). Despite the major dehydration, significant amounts of water may be retained inside the subducted slab and reach the MTZ (Ohtani et al., 2004). Once the slab reaches the MTZ, two types of behavior can be observed (Goes et al., 2017): (i) direct slab penetration into the lower mantle (LM) and

©2020. The Authors.

This is an open access article under the terms of the Creative Commons Attribution License, which permits use, distribution and reproduction in any medium, provided the original work is properly cited.

(ii) slab stagnation within the MTZ. Whichever the case, continuous slab heating could progressively decompose water-bearing phases hosted in the subducted lithosphere, causing local hydration of the MTZ (Richard et al., 2006). The amount of water released by the sinking slab into the MTZ depends on its residence time in this region, and on how fast heat transfers through the lithosphere. Typically, the warmer the slab is after its residence in the MTZ, the more water is released. In reverse, with lower slab temperatures, the amount of water retained in its interior will be larger.

Lattice thermal conductivity, Λ_{lat} , of mantle minerals is a key parameter that controls heat transfer through the mantle, which in turn determines the thermal states and geodynamics of planets (Zhang et al., 2019). In particular, for hydrous minerals in the MTZ and subducting slabs, knowledge of the effects of pressure P , temperature T , and water content $C_{\text{H}_2\text{O}}$ on their lattice thermal conductivities are fundamental to constrain the thermal interactions between the hydrated slab and the MTZ. However, due to experimental difficulties, it remains largely unknown how Λ_{lat} of hydrous minerals varies with potential P , T and $C_{\text{H}_2\text{O}}$ in the mantle. Recently, Chang et al. (2017) reported that, compared to the anhydrous counterpart, the presence of 0.7 wt% of water significantly reduces the lattice thermal conductivity of San Carlos olivine by a factor of ≈ 2 at the pressures near the MTZ. Given its large water storage capacity and its abundance in the MTZ, the effects of P and $C_{\text{H}_2\text{O}}$ on ringwoodite thermal conductivity are essential to determine the inner temperatures of subducting slabs.

In this study, we couple diamond-anvil cell (DAC) experiments with ultrafast time domain thermoreflectance (TDTR) to determine the P and $C_{\text{H}_2\text{O}}$ dependencies of ringwoodite thermal conductivity, Λ_{RW} , at MTZ pressures and room temperature. Combining our measurements with finite-difference numerical modeling, we show that the hydration-reduced Λ_{RW} prolongs the time required to reach thermal equilibrium within a subducting slab, thus enabling temperature-sensitive hydrous minerals to be transported to greater depth. Our results demonstrate the importance of hydration on the thermal evolution and fate of descending slabs.

2. Materials and Experimental Methods

2.1. Sample Synthesis and Characterization

Natural San Carlos olivine (SCO) was used as a starting material to synthesize ringwoodite samples. A large SCO crystal was crushed into fine powders after selecting grains without inclusions. Ringwoodite with increasing $C_{\text{H}_2\text{O}}$ was synthesized using 1,000- and 1,200-t multianvil presses at the Bayerisches Geoinstitut (BGI), University of Bayreuth, Germany (Table S1 in the supporting information). For dry ringwoodite synthesis the SCO powder was packed into a Re foil capsule, whereas for hydrous experiments we added distilled water (3–10 wt%) into a Pt₉₅Rh₅ capsule, later sealed by welding. Each capsule was then slid into an MgO sleeve, which was surrounded by a LaCrO₃ heater, and a ZrO₂ thermal insulator. The whole assembly was loaded into a 5 wt% Cr₂O₃-doped MgO octahedron with 10-mm edge length. Mo electrodes were located at both ends of the heater. Finally, we combined the pressure vessel with second-stage tungsten carbide anvils with 4-mm truncation (ha-7%Co, Hawedia; e.g., Ishii, Liu, & Katsura, 2019). The ceramic parts of the pressure vessel were heated for more than 3 hr at 1273 K before assembly. Dry ringwoodite was synthesized at 22 GPa and 1900 K for 1.25 hr, whereas the hydrous samples were obtained after 3–8 hr at 20–22 GPa and 1600–1700 K. The sample was first compressed to the desired press load and then heated to the target temperature. After maintaining a constant temperature for several hours, the sample was quenched by turning off the electrical power. Temperature was estimated based on empirical power-temperature relations obtained in separate runs. The resulting hydrous batches contained single crystals of ringwoodite (>100 μm), whereas the dry batch contained a polycrystalline aggregate composed by crystals with a size of a few tens of microns.

After retrieval, we selected ringwoodite crystals based on clear crystal morphology under an optical microscope. Furthermore, we performed single crystal X-ray diffraction (XRD) analysis to confirm the quality of the ringwoodite samples. XRD analyses were performed by employing a Huber four-circle diffractometer, driven by the SINGLE software (Angel & Finger, 2011), equipped with a point detector, and a Mo-K α source, which was operated at 50 kV and 40 mA. Only ringwoodite crystals with a full width at half maximum of <0.1 $^\circ$, upon omega-scan rotation, were selected for our thermal conductivity measurements.

We further used unpolarized Fourier transform infrared (FTIR) spectroscopy to measure the water weight concentration $C_{\text{H}_2\text{O}}$ of the synthesized batches. For each batch we selected one representative crystal, and double-side polished it to a thickness of $\approx 15\text{--}30\ \mu\text{m}$. $C_{\text{H}_2\text{O}}$ was derived using the Lambert-Beer law, by employing a molar absorption coefficient ϵ of $106,002\ \text{L mol}^{-1}\ \text{cm}^{-2}$ (Thomas et al., 2015). We considered $C_{\text{H}_2\text{O}}$ in each batch to be nearly the same, due to water oversaturated conditions during synthesis. From our FTIR measurements, $C_{\text{H}_2\text{O}}$ of synthesized batches are as follows: 0.11, 0.47, and 1.73 wt% (Table S2). These values typically have $\approx 30\%$ uncertainty (Thomas et al., 2015). We employed electron probe microanalysis (EPMA) to determine the composition of the selected samples. All the measurements were performed using a JEOL Superprobe JXA-8200 at BGI. The amounts of silicon, magnesium, and iron were measured using the olivine standard (Mg, Fe, and Si). Samples were coated with a 12-nm carbon film. We found that the synthesized ringwoodite contains $\approx 8.5\ \text{wt}\%$ FeO on average, with a $100\ \text{MgO}/(\text{MgO} + \text{FeO})$ value of 91.7. The chemical formula calculated from EPMA data is $[\text{Mg}_{1.79}\text{Fe}_{0.17}\text{Si}_{1.02}\text{O}_4]$. The position of H^+ in the hydrous ringwoodite structure, depends on the $(\text{Mg} + \text{Fe})/\text{Si}$ ratio. With increasing $(\text{Mg} + \text{Fe})/\text{Si}$ and increasing water content H^+ is almost exclusively hosted in Mg sites (Fei & Katsura, 2019), confirmed for our samples by EMPA measurements (Table S3). As reported in McCammon et al. (2004), the $\text{Fe}^{3+}/\Sigma\text{Fe}$ ratio in ringwoodite is relatively low and stabilizes around ≈ 0.15 , even in oxidizing conditions. Moreover, Schulze et al. (2018) found almost no correlation between hydration and capsule material and the measured $\text{Fe}^{3+}/\Sigma\text{Fe}$ ratio (0.1–0.18%). Therefore, we assumed a homogeneous Fe^{3+} content in our samples.

2.2. High-Pressure Lattice Thermal Conductivity Measurements

To perform thermal conductivity measurements, ringwoodite samples were first polished down to $\approx 25\ \mu\text{m}$ thickness and then coated with $\approx 90\text{-nm}$ -thick Al film as a thermal transducer for TDTR measurements. Each sample was loaded into a symmetric piston-cylinder DAC with $400\text{-}\mu\text{m}$ -culet diamonds and a Re gasket. Silicone oil (CAS No. 63148-62-9 from Acros Organics) was used as the pressure medium due to its exceptionally low thermal conductivity at high pressures, which considerably reduces the measurement uncertainty (Hsieh, 2015). Pressure inside the DAC was estimated by ruby fluorescence (Mao et al., 1986), which gives an uncertainty of typically $<5\%$.

We used TDTR to measure the lattice thermal conductivity of ringwoodite Λ_{RW} at high pressures and room temperature. TDTR coupled with DAC is a well-developed, ultrafast optical pump-probe metrology to precisely measure the thermal conductivity of materials at extremely high-pressure conditions (Hsieh et al., 2017, 2018). In the TDTR measurement, the output of a Ti:sapphire laser is split into pump and probe beams (Hsieh et al., 2009). The pump beam heats up the Al coated onto the sample, causing temperature variations. As the excess heat transfers into the sample and the silicone oil, the temperature evolution of the Al film is monitored by measuring the small variations in the reflected probe beam intensity that is synchronized with the 8.7 MHz modulation frequency of the pump beam. The small variations of the reflected probe beam intensity, including the in-phase V_{in} and out-of-phase V_{out} components, are measured using a Si photodiode and a lock-in amplifier. The detailed setup and principles of TDTR are described in Cahill (2004), Chao (2018), and Kang et al. (2008).

To determine the Λ_{RW} we compared the ratio $-V_{\text{in}}/V_{\text{out}}$ as a function of time delay between the pump and probe beams, with the numerical calculations obtained from a bidirectional thermal model that takes into account the heat flow into the sample and the silicone oil (Cahill & Watanabe, 2004; Schmidt et al., 2008; Zheng et al., 2007). This model requires the input of several parameters—thermal conductivity Λ_{lat} , volumetric heat capacity C , and thickness h for each layer (i.e., silicone oil, Al film, and ringwoodite), while Λ_{RW} is the only significant unknown and free parameter to be determined. At ambient pressure, the thermal conductivity of the Al film Λ_{Al} is high ($\approx 200\ \text{W m}^{-1}\ \text{K}^{-1}$), and its increase at high pressures has a negligible effect on the thermal model calculations. Therefore, Λ_{Al} is assumed to be a constant at high pressures. Pressure dependencies of the silicone oil thermal conductivity $\Lambda_{\text{Si oil}}$, volumetric heat capacity $C_{\text{Si oil}}$, as well as the Al volumetric heat capacity C_{Al} were taken from Hsieh et al. (2009) and Hsieh (2015). The ringwoodite volumetric heat capacity C_{RW} was obtained from Dorogokupets et al. (2015). Prior studies have indicated that the effect of impurities on the volumetric heat capacity of a material is typically very small if the impurity concentration is $\leq 10\ \text{at}\%$ (Chang et al., 2017; Fukui et al., 2012). Given the relatively small amount of water in ringwoodite (only up to $\approx 9.5\ \text{at}\%$ per formula unit), we assumed that hydrous C_{RW} is equal to the

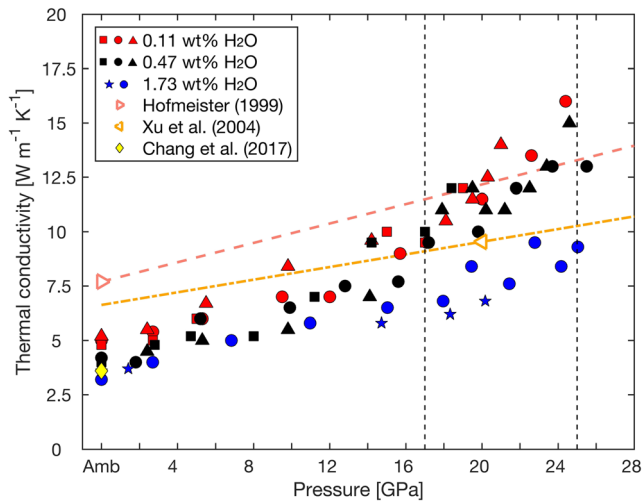


Figure 1. Pressure (P) evolution of Λ_{Rw} for different C_{H_2O} at room temperature ($T = 298$ K). Each experimental run is identified by a distinct symbol (Table S5), whereas C_{H_2O} is marked by color: 0.11 wt% (red), 0.47 wt% (black), and 1.73 wt% (blue). Within the pressure range relevant to the lower MTZ (vertical dashed lines), $\Lambda_{1.73}$ is $\approx 40\%$ lower than $\Lambda_{0.11}$. Amb stands for ambient pressure. Literature data for nominally dry Λ_{Rw} are identified by open markers, together with their relative extrapolation (dashed lines). Data by Chang et al. (2017) for nominally dry Λ_{OI} is also plotted for comparison.

the 10–15% reduction observed in $\Lambda_{0.47}$ is comparable to our measurement uncertainty. The incorporation of 1.73 wt% water, however, clearly shows a detectable difference in Λ_{Rw} , indicating a strong reduction of thermal conductivity due to the hydration effect at ambient conditions. Upon compression, the ratio of $\Lambda_{0.47}$ to $\Lambda_{0.11}$ remains approximately a constant (black curve in Figure S3). However, the hydration-induced reduction of Λ_{Rw} with 1.73 wt% water enhances with pressure, reaching $>40\%$ reduction at the MTZ pressures (Figures 1 and S3). In ringwoodite, water is incorporated into its defect sites in the form of hydroxyl group (OH^-) or proton (H^+) by replacing cations (Si^{4+} , Mg^{2+} , and Fe^{2+}) (Grüniger et al., 2017; Panero et al., 2013). As pressure increases, the interatomic distance shortens, and these ionic defects may form an interconnected network that acts as an additional phonon-defect scattering mechanism (Chang et al., 2017). This effect promotes scattering of thermal energy carriers and reduces the phonon mean-free-path, hindering the thermal energy transport. Hence, the presence of ionic defects (in our case due to water incorporation) results in the pressure-induced suppression of Λ_{lat} . A similar effect has been reported for water-bearing olivine (Chang et al., 2017). Compared to its effect on sound velocity, where v_P and v_S of ringwoodite decrease only by $\approx 0.25\%$ at $C_{H_2O} = 0.5$ wt% (Schulze et al., 2018), the proton weakening has a significant effect on Λ_{Rw} . Note that for the polycrystalline dry samples, the measured Λ_{Rw} are obtained by averaging several measurements at different locations on the sample probed by the laser with a spot size of $15 \mu\text{m}$ in diameter. The effect of grain boundaries on Λ_{lat} in our samples should be minor, since the grain size is larger than $10 \mu\text{m}$ (Liang, 2017).

To parameterize the effect of pressure on Λ_{Rw} with different C_{H_2O} , we fitted our data (Tables S6–S8) with a second-order polynomial: $\Lambda_{Rw}(P) = qP^2 + lP + \Lambda_0$, where $\Lambda_{Rw}(P)$ is the thermal conductivity at a given pressure, Λ_0 the thermal conductivity at ambient pressure, q and l the quadratic and linear coefficient, respectively. The coefficients for each fit are reported in Tables S6–S8. To quantify the combined effects of hydration and pressure, we employed a linear interpolation between the parameterized curves for $\Lambda_{0.11}(P)$, $\Lambda_{0.47}(P)$, and $\Lambda_{1.73}(P)$ (Table S9 and Figure S4). We found that Λ_{Rw} as function of C_{H_2O} and P can be expressed as $\Lambda_{Rw}(C_{H_2O}, P) = a(P)C_{H_2O} + \Lambda_{Dry}(P)$, where C_{H_2O} is the water content in ppm, $a(P)$ the pressure-dependent linear parameter (Table S10 and Figure S5), and $\Lambda_{Dry}(P)$ the intercept for 0 ppm (Table S10 and Figure S6). Pressure dependence of the coefficient a can be described by a second-order polynomial: $a(P) = bP^2 + cP + a_0$, as well as $\Lambda_{Dry}(P): \Lambda_{Dry}(P) = dP^2 + eP + \Lambda_0$. A total of six different coefficients

anhydrous one. The thickness of the Al film h_{Al} at ambient pressure was measured by picosecond acoustics (O'Hara et al., 2001). However, the acoustic signal becomes too weak to be used to derive h_{Al} during compression. Thus, we estimated h_{Al} squeezing by employing the method developed by Chen et al. (2011). Since under our experimental conditions the thermal penetration depths of ringwoodite and silicone oil are both on the order of only few hundreds of nanometers (Hsieh et al., 2009), the thermal model calculation is insensitive to their thicknesses h_{Rw} and $h_{Si\text{ oil}}$ ($\approx 25 \mu\text{m}$). A set of example data with the calculations from the thermal model is reported in Figure S1 and Table S4. To determine the error propagation in Λ_{Rw} , we performed sensitivity tests for the heat diffusion thermal model by varying each input parameter (Figure S2). From our sensitivity tests, the estimated error ranges between $\approx 10\%$ ($P \leq 15$ GPa) and $\approx 15\%$ ($15 \text{ GPa} < P < 25$ GPa).

3. Experimental Results and Discussion

TDTR measurements were performed at room temperature and high pressures for three different C_{H_2O} values: low (0.11 wt%), medium (0.47 wt%), and high (1.73 wt%) (Figure 1 and Table S5). The ringwoodite stability field ranges between 17–24 GPa (e.g., Ishii et al., 2011; Litasov et al., 2006), and therefore, pressure points are closely spaced within this range.

For clarity, we indicate Λ_{Rw} for different C_{H_2O} with the symbols $\Lambda_{0.11}$, $\Lambda_{0.47}$, and $\Lambda_{1.73}$. At ambient pressure, $\Lambda_{0.47}$ is $\approx 10\text{--}15\%$ smaller than $\Lambda_{0.11}$, whereas $\Lambda_{1.73}$ shows a 30% reduction compared to $\Lambda_{0.11}$. Note that

has to be established in order to calculate Λ_{Rw} as a function of $C_{\text{H}_2\text{O}}$ (in ppm) and P (in GPa). From our TDTR measurements we derived the following relation (Table S11):

$$\Lambda_{\text{Rw}}(C_{\text{H}_2\text{O}}, P) = (-7 \times 10^{-7} P^2 + 4 \times 10^{-6} P - 9 \times 10^{-5}) C_{\text{H}_2\text{O}} + 1.37 \times 10^{-2} P^2 + 1.055 \times 10^{-1} P + 4.8403$$

This equation describes Λ_{Rw} well within the tested experimental range ($C_{\text{H}_2\text{O}} = 0\text{--}1.73$ wt%; $P = 0\text{--}25$ GPa), showing <7% discrepancy from our measurements (within experimental errors) (Figures S7–S10). Note that we assumed a progressive $C_{\text{H}_2\text{O}}$ effect on Λ_{Rw} , without including any sharp threshold above which the presence of water causes major reduction in Λ_{Rw} .

Based on our empirical equation Λ_{Rw} is $4.84 \text{ W m}^{-1} \text{ K}^{-1}$, for $C_{\text{H}_2\text{O}} = 0$ wt% and $P = 10^{-4}$ GPa (1 atm), whereas it is $12.4 \text{ W m}^{-1} \text{ K}^{-1}$ at 20 GPa and 0 wt% H_2O (Table S9). Our estimates are about 40% lower compared to the result obtained by infrared reflectivity measurements of Hofmeister (1999) for dry Mg_2SiO_4 ringwoodite. The difference may be due to the difference in FeO content of the ringwoodite, which lowers thermal conductivity of minerals (Hsieh et al., 2018, 2020). Xu et al. (2004) reported $\Lambda_{\text{Rw}} = 9.54 \text{ W m}^{-1} \text{ K}^{-1}$ ($C_{\text{H}_2\text{O}} = 0$ wt%, $P = 20$ GPa) measured using the in situ Ångström method. Our Λ_{Rw} estimated at the same conditions is 25% higher. Xu et al. (2004) report that the olivine thermal conductivity Λ_{Ol} is 30% lower than Λ_{Rw} . This result is coherent with the $\Lambda_{\text{Ol}}/\Lambda_{\text{Rw}}$ ratio obtained here, when the previous Λ_{Ol} from Chang et al. (2017) is used. Note that both measurements were acquired with the same TDTR technique. The discrepancy between our results and those by Xu et al. (2004) might be explained by their experimental techniques, the Ångström method, which relies on proper contacts between thermocouples and sample. In contrast, the TDTR method is based on a noncontact optical technique, avoiding this potential problem and possibly resulting in different Λ_{Rw} values.

4. Potential Impact on the Thermal Structure of Subducting Slabs

4.1. Hydration of MTZ

In recent years, the amount and spatial distribution of water in the mantle has been under debate (Ohtani, 2019). Understanding the deep Earth water cycle, along with physical properties of hydrous minerals, is essential to understand the long-term evolution of the Earth's mantle. Thermopetrological simulations performed by van Keken et al. (2011) estimated that one third of the initial slab water content is able to reach MTZ depths. In these models, the preserved water is mainly hosted in the cold inner regions of the slab (e.g., lower crust and upper lithospheric mantle). Following these considerations, it becomes clear that the thermal evolution of the slab determines where and how much water is released during subduction. Variations in thermal properties of slab minerals might be responsible for the heterogenous hydration state of different mantle regions. Chang et al. (2017) reported that the hydration-reduced thermal conductivity of the crustal materials can induce a low-temperature anomaly in the slab interior. Potentially, this effect might preserve hydrous minerals to be transported to greater depth by maintaining a colder slab core. The water-bearing phase in a slab located in the MTZ are expected to consist of nominally anhydrous minerals (e.g., wadsleyite and ringwoodite) and dense hydrous magnesium silicates (DHMS, such as superhydrous Phase B or Phase D) (Ohtani et al., 2004). Once ringwoodite reaches the base of the MTZ, it decomposes into LM assemblage (e.g., Ishii et al., 2018; Ishii, Huang, et al., 2019; Ishii, Kojitani, & Akaogi, 2019; Litasov et al., 2005), which is expected to host only $\approx 1,000$ ppm of water (Fu et al., 2019; Litasov et al., 2003). Due to the release of water around 660-km depth, this decomposition most likely causes major slab dehydration (Schmandt et al., 2014). A possible way to deliver water down to the LM is via subduction of DHMS. These phases are stable at high pressure (up to 40 GPa) but are extremely sensitive to high temperatures since they decompose at $\approx 1,500$ K (Ohtani et al., 2004); however, so far, it remains unclear whether DHMS can reach the LM.

4.2. Numerical Modeling

To assess the impact of a reduced Λ_{Rw} on a slab's thermal evolution, we employed a self-written 1-D finite difference heat diffusion model. We modeled an 80 Myr old slab (116.8 km thick) that stagnates at 660-km depth. The warmer ambient mantle heats the slab from the upper and lower boundaries. For simplicity the oceanic lithosphere was assumed to be chemically homogeneous. The model domain was discretized using 1,169 nodal points, corresponding to a grid spacing of 100 m.

We established the initial temperature profile of the stagnating slab using a two stage calculation: (1) We computed the temperature field of an 80 Myr old slab using the analytical solution for half-space cooling (Turcotte & Schubert, 2014); (2) we simulated the thermal evolution of the subducting slab from the trench down to the MTZ by assuming a sinking time t_{sink} of 10 Myr (Table S12) using the 1-D finite difference heat diffusion model. This sinking time is comparable to those of several subduction zones, such as North and South Kurile (Syracuse et al., 2010). Frictional heating and complex interactions between the slab and overriding plate were neglected for simplicity. The average thermal diffusivity κ during the slab descent was calculated based on literature data for thermal conductivity Λ_{OI} (Chang et al., 2017), density ρ_{OI} (Zhang & Bass, 2016), and specific heat capacity $C_{\text{P OI}}$ (Su et al., 2018) of olivine (Table S12). As we focus on the impact of hydrous ringwoodite on the thermal evolution, we did not take into account any hydration reduction of Λ_{lat} at this stage. We neglected adiabatic compression, and therefore the ambient mantle temperature was fixed at 1600 K at any depth. The temperature structure of the slab at the end of the descent to the MTZ is shown in Figure S13 and was used as initial temperature condition for all simulations described below.

Once the initial temperature profile was defined, we studied slab heating during potential stagnation in the lower MTZ (540–660 km). Previous works estimated stagnation times t_{stag} to range from 50 to 140 Myr (Fukao et al., 2009; Richard et al., 2006; Zhao, 2004), and thus, we ran our simulations for 150 Myr. This simulation time was chosen to include all estimates of stagnation age, since slab avalanche phenomena were not considered in our models. During the stagnation stage, we assumed that the slab is entirely composed of ringwoodite. Pressure and water dependence of Λ_{RW} were based on the empirical equation derived in this study. In order to properly study thermal evolution of the slab crossing the MTZ it is fundamental to use a P - T -dependent Λ_{RW} (Xu et al., 2004), ρ_{RW} (Ye et al., 2012) and $C_{\text{P RW}}$ (Dorogokupets et al., 2015; Saxena, 1996) to calculate thermal diffusivity κ (Text S2). As an approximation, two end-member parameters settings were used in our simulations: one given by the lowest temperature in the slab core (1021 K), and the other given by the ambient mantle temperature (1600 K).

To reproduce the effect of hydrous Λ_{RW} on a slab's thermal evolution, we prescribed a hydrous layer in the uppermost part of the slab. Following our TDTR measurements, this hydrous layer acts as a heat propagation buffer. To simulate the hydrous region, we defined two parameters: hydrous layer thickness D_{hyd} , and its water content $C_{\text{H}_2\text{O}}$. The rest of the slab was considered to be dry. In our model settings we ignored the additional contribution of radiative thermal conductivity Λ_{rad} on the total heat transport (Thomas et al., 2012), and the presence of garnetitic crust in the upper part of the slab (Giesting et al., 2004; Irifune & Ringwood, 1993). Detailed limitations of our numerical model are discussed in the supplementary material (Texts S1–S3).

The oceanic lithosphere reacts with seawater at the mid-ocean ridge (hydrothermal circulation) and in trench-rise systems (water percolation) (Ranero et al., 2003). Thus, lithosphere hydration may reach 20-km depth (Green et al., 2010), and it might extend further down to 40-km depth due to the pressure gradient caused by slab unbending (Faccenda et al., 2012). Therefore, we chose values for D_{hyd} ranging from 5 up to 40 km. Despite the high-water solubility of ringwoodite of 1.5–2 wt% (Inoue et al., 2010), it is unlikely that such a large amount of water is hosted pervasively in the slab (Karato, 2011; Koyama et al., 2006; Suetsugu et al., 2010; Yoshino et al., 2008). Thus, we applied an upper limit of $C_{\text{H}_2\text{O}} = 1.5$ wt%, consistent with a natural ringwoodite sample (Pearson et al., 2014). We performed a total of 242 simulations covering 150 Myr of slab stagnation in the MTZ. As the reference case we used a completely dry slab: $D_{\text{hyd}} = 0$ km, $C_{\text{H}_2\text{O}} = 0$ wt% (Figure S14).

Based on our models, it takes ≈ 80 –110 Myr to reach 99% of mantle temperature for a completely dry slab. Complete thermal equilibration is not achieved within the 150 Myr time span, and the presence of a hydrous layer significantly delays heat propagation. To study the effects of this delay, we computed the time t_{crit} it takes to reach a critical temperature T_{crit} of 1500 K at the base of the hydrous layer, assuming that this will mark the complete decomposition of DHMS (Ohtani et al., 2004). For each simulation we calculated the delay time t_{delay} , defined as the difference between t_{crit} for hydrated slabs and the time it takes to reach T_{crit} at the relevant depth inside a completely dry slab (Figure 2 and Tables S14 and S15).

The most pronounced delay can be observed for $15 \text{ km} < D_{\text{hyd}} < 20 \text{ km}$, reaching its maximum at $C_{\text{H}_2\text{O}} = 1.5$ wt% ($t_{\text{delay}} = 20$ –27 Myr). Fei and Katsura (2019) reported that ringwoodite water solubility

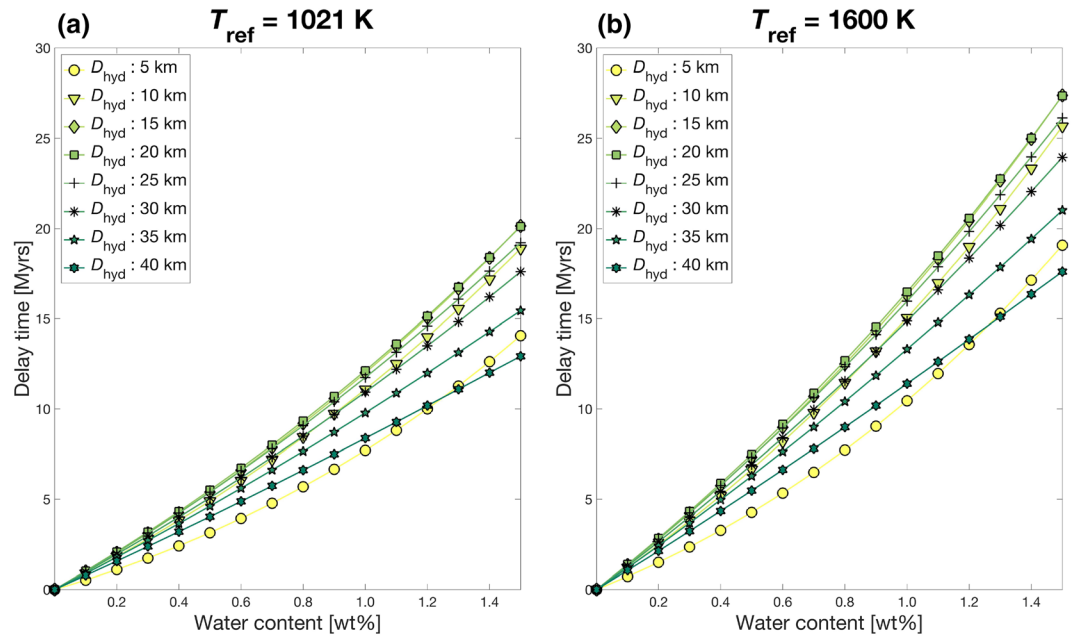


Figure 2. Comparison of delay time for different D_{hyd} and $C_{\text{H}_2\text{O}}$ combinations assuming $T_{\text{crit}} = 1500$ K. Each subplot is based on a separate set of models where thermal diffusivity κ was calculated using end-member reference temperatures: (a) $T_{\text{ref}} = 1021$ K and (b) $T_{\text{ref}} = 1600$ K.

at MTZ temperatures (1950–2000 K) is ≈ 0.8 –1.2 wt%. For a hydrous layer of 15–20 km thickness containing 0.8–1.2 wt% water, t_{delay} ranges from 9 to 20 Myr (Figure 2). This delay might be crucial to hinder slab heating and DHMS breakdown, allowing them to be transported to greater depth in the LM as even a slowly descending slab with $v_{\text{sink}} = 1$ cm yr $^{-1}$ (Van Der Meer et al., 2010) will sink through the MTZ within ≈ 25 Myr. For a dry slab, the 1500 K isotherm will penetrate to 10–15 km depth within this time frame (Tables S14 and S15). The effect of 1 wt% water within this layer results in a 12–15 Myr delay of DHMS breakdown (Figure 2). Our modeling results indicate that the hydrated ringwoodite can have a significant impact on the thermal evolution of descending slabs and thus needs to be taken into account when modeling their thermal structures.

5. Conclusions

The effect of water on Λ_{RW} found in our experiments offers novel insights into the thermal evolution of subducting slabs and the fate of hydrous minerals. From TDTR analysis we determined a Λ_{RW} reduction of up to 40% at pressures relevant for the MTZ. We parameterized water and pressure dependencies of Λ_{RW} . Our empirical equation combined with finite difference numerical modeling shows that a homogeneously hydrated layer on top of a slab results in a slower heat propagation through its interior. The delay time caused by the reduced Λ_{RW} provides a potential water-preserving mechanism that prolongs the lifetime of DHMS, enabling them to be transported into the LM. The hydration-reduced thermal conductivity of ringwoodite and olivine (Chang et al., 2017) is expected to be relevant for other water-bearing minerals (e.g., DHMS and wadsleyite). Importantly, the temperature influences not only the stability field of minerals but also key physical properties, such as density and viscosity. Thus, including our findings into a more detailed thermochemical model would substantially advance our understanding of the thermal evolution of subduction zones.

Data Availability Statement

Data are available via the figshare repository: <https://figshare.com/s/f6cec9cfd5482116918> (1-D code), <https://figshare.com/s/96af714f5afc582fb5ec> (figures), and <https://figshare.com/s/67901c34907d49baf4b2> (tables).

Acknowledgments

We thank Hana Čížková and an anonymous reviewer for their constructive comments that helped to improve the manuscript considerably. This study has been supported by DFG (Grant GRK 2156/1) and the JSPS Japanese-German graduate externship. Additional support was received from Academia Sinica and the Ministry of Science and Technology (MOST) of Taiwan, Republic of China, under Contract AS-CDA-106-M02 and 107-2628-M-001-004-MY3. T. I. was funded by an Alexander von Humboldt Postdoctoral Fellowship and the German Research Foundation (DFG) (IS350/1-1). M. T. was supported by the Bayerisches Geoinstitut Visitor's Program. E. O. was supported by the Kakenhi Grant JP15H05748 from Japan Society for the Promotion of Science, and by the research award from the Alexander von Humboldt foundation. W.-P. H. acknowledges the fellowship from the Foundation for the Advancement of Outstanding Scholarship, Taiwan. We thank T. Boffa-Ballaran, G. Criniti, and A. I. Landi for their help with XRD measurements; H. Keppler for his help with FTIR measurements; and D. Krauß and S. Abeykoon for their expertise in EPMA measurements. We also thank R. Njul and A. E. Rother for sample preparation, and C.-C. Chen and Y.-C. Tsao at Academia Sinica for their help with the experiments.

References

Angel, R. J., & Finger, L. W. (2011). SINGLE: A program to control single-crystal 206 diffractometers. *Journal of Applied Crystallography*, *44*(1), 247–251. <https://doi.org/10.1107/S0021889810042305>

Cahill, D. G. (2004). Analysis of heat flow in layered structures for time-domain thermoreflectance. *Review of Scientific Instruments*, *75*(12), 5119–5122. <https://doi.org/10.1063/1.1819431>

Cahill, D. G., & Watanabe, F. (2004). Thermal conductivity of isotopically pure and Ge-doped Si epitaxial layers from 300 to 550 K. *Physical Review B*, *70*(23), 235322. <https://doi.org/10.1103/PhysRevB.70.235322>

Chang, Y. Y., Hsieh, W. P., Tan, E., & Chen, J. (2017). Hydration-reduced lattice thermal conductivity of olivine in Earth's upper mantle. *Proceedings of the National Academy of Sciences*, *114*(16), 4078–4081. <https://doi.org/10.1073/pnas.1616216114>

Chao, K.-H. (2018). Spin transition and thermal conductivity of (Fe_{0.78}Mg_{0.22}CO₃) siderite under high pressure. *MSc thesis*. National Central University.

Chen, B., Hsieh, W. P., Cahill, D. G., Trinkle, D. R., & Li, J. (2011). Thermal conductivity of compressed H₂O to 22 GPa: A test of the Leibfried-Schlömann equation. *Physical Review B*, *83*(13), 132301. <https://doi.org/10.1103/PhysRevB.83.132301>

Dorogokupets, P. I., Dymshits, A. M., Sokolova, T. S., Danilov, B. S., & Litasov, K. D. (2015). The equations of state of forsterite, wadsleyite, ringwoodite, akimotoite, MgSiO₃-perovskite, and postperovskite and phase diagram for the Mg₂SiO₄ system at pressures of up to 130 GPa. *Russian Geology and Geophysics*, *56*(1–2), 172–189. <https://doi.org/10.1016/j.rgg.2015.01.011>

Faccenda, M. (2014). Water in the slab: A trilogy. *Tectonophysics*, *614*, 1–30. <https://doi.org/10.1016/j.tecto.2013.12.020>

Faccenda, M., Gerya, T. V., Mancktelow, N. S., & Moresi, L. (2012). Fluid flow during slab unbending and dehydration: Implications for intermediate-depth seismicity, slab weakening and deep water recycling. *Geochemistry, Geophysics, Geosystems*, *13*(1), Q01010. <https://doi.org/10.1029/2011GC003860>

Fei, H., & Katsura, T. (2019). High water solubility of ringwoodite at mantle transition zone temperature. *Earth and Planetary Science Letters*, *531*, 115987. <https://doi.org/10.1016/j.epsl.2019.115987>

Frost, D. J. (2008). The upper mantle and transition zone. *Elements*, *4*(3), 171–176. <https://doi.org/10.2113/GSELEMENTS.4.3.171>

Fu, S., Yang, J., Karato, S. I., Vasiliev, A., Presniakov, M. Y., Gavriluk, A. G., et al. (2019). Water concentration in single-crystal (Al, Fe)-bearing Bridgmanite grown from the hydrous melt: Implications for dehydration melting at the topmost lower mantle. *Geophysical Research Letters*, *46*(17–18), 10,346–10,357. <https://doi.org/10.1029/2019GL084630>

Fukao, Y., Obayashi, M., Nakakuki, T., & Deep Slab Project Group (2009). Stagnant slab: A review. *Annual Review of Earth and Planetary Sciences*, *37*(1), 19–46. <https://doi.org/10.1146/annurev.earth.36.031207.124224>

Fukui, H., Tsuchiya, T., & Baron, A. Q. R. (2012). Lattice dynamics calculations for ferropericlae with internally consistent LDA + U method. *Journal of Geophysical Research*, *117*, B12202. <https://doi.org/10.1029/2012JB009591>

Giesting, P. A., Hofmeister, A. M., Wopenka, B., Gwanmesia, G. D., & Jolliff, B. L. (2004). Thermal conductivity and thermodynamics of majoritic garnets: Implications for the transition zone. *Earth and Planetary Science Letters*, *218*(1–2), 45–56. [https://doi.org/10.1016/S0012-821X\(03\)00630-7](https://doi.org/10.1016/S0012-821X(03)00630-7)

Goes, S., Agrusta, R., van Hunen, J., & Garel, F. (2017). Subduction-transition zone interaction: A review. *Geosphere*, *13*(3), 644–664. <https://doi.org/10.1130/GES01476.1>

Green, H. W. II, Chen, W. P., & Brudzinski, M. R. (2010). Seismic evidence of negligible water carried below 400-km depth in subducting lithosphere. *Nature*, *467*(7317), 828–831. <https://doi.org/10.1038/nature09401>

Grüninger, H., Armstrong, K., Greim, D., Boffa-Ballaran, T., Frost, D. J., & Senker, J. (2017). Hidden oceans? Unraveling the structure of hydrous defects in the Earth's deep interior. *Journal of the American Chemical Society*, *139*(30), 10,499–10,505. <https://doi.org/10.1021/jacs.7b05432>

Hofmeister, A. M. (1999). Mantle values of thermal conductivity and the geotherm from phonon lifetimes. *Science*, *283*(5408), 1699–1706. <https://doi.org/10.1126/science.283.5408.1699>

Hsieh, W.-P. (2015). Thermal conductivity of methanol-ethanol mixture and silicone oil at high pressures. *Journal of Applied Physics*, *117*(23), 235901. <https://doi.org/10.1063/1.4922632>

Hsieh, W.-P., Chen, B., Li, J., Koblinski, P., & Cahill, D. G. (2009). Pressure tuning of the thermal conductivity of the layered muscovite crystal. *Physical Review B*, *80*(18), 180302. <https://doi.org/10.1103/PhysRevB.80.180302>

Hsieh, W.-P., Deschamps, F., Okuchi, T., & Lin, J. F. (2017). Reduced lattice thermal conductivity of Fe-bearing bridgmanite in Earth's deep mantle. *Journal of Geophysical Research: Solid Earth*, *122*, 4900–4917. <https://doi.org/10.1002/2017JB014339>

Hsieh, W.-P., Deschamps, F., Okuchi, T., & Lin, J. F. (2018). Effects of iron on the lattice thermal conductivity of Earth's deep mantle and implications for mantle dynamics. *Proceedings of the National Academy of Sciences*, *115*(16), 4099–4104. <https://doi.org/10.1073/pnas.1718557115>

Hsieh, W. P., Ishii, T., Chao, K. H., Tsuchiya, J., Deschamps, F., & Ohtani, E. (2020). Spin transition of iron in δ-(Al, Fe) OOH induces thermal anomalies in Earth's lower mantle. *Geophysical Research Letters*, e2020GL087036. <https://doi.org/10.1029/2020GL087036>

Inoue, T., Wada, T., Sasaki, R., & Yurimoto, H. (2010). Water partitioning in the Earth's mantle. *Physics of the Earth and Planetary Interiors*, *183*(1–2), 245–251. <https://doi.org/10.1016/j.pepi.2010.08.003>

Irfune, T., & Ringwood, A. E. (1987). Phase transformations in a harzburgite composition to 26 GPa: Implications for dynamical behaviour of the subducting slab. *Earth and Planetary Science Letters*, *86*(2–4), 365–376. [https://doi.org/10.1016/0012-821X\(87\)90233-0](https://doi.org/10.1016/0012-821X(87)90233-0)

Irfune, T., & Ringwood, A. E. (1993). Phase transformations in subducted oceanic crust and buoyancy relationships at depths of 600–800 km in the mantle. *Earth and Planetary Science Letters*, *117*(1–2), 101–110. [https://doi.org/10.1016/0012-821X\(93\)90120-X](https://doi.org/10.1016/0012-821X(93)90120-X)

Ishii, T., Huang, R., Fei, H., Koemets, I., Liu, Z., Maeda, F., et al. (2018). Complete agreement of the post-spinel transition with the 660-km seismic discontinuity. *Scientific Reports*, *8*(1), 6358–6356. <https://doi.org/10.1038/s41598-018-24832-y>

Ishii, T., Huang, R., Myhill, R., Fei, H., Koemets, I., Liu, Z., et al. (2019). Sharp 660-km discontinuity controlled by extremely narrow binary post-spinel transition. *Nature Geoscience*, *12*(10), 869–872. <https://doi.org/10.1038/s41561-019-0452-1>

Ishii, T., Kojitani, H., & Akaogi, M. (2011). Post-spinel transitions in pyrolite and Mg₂SiO₄ and akimotoite–perovskite transition in MgSiO₃: Precise comparison by high-pressure high-temperature experiments with multi-sample cell technique. *Earth and Planetary Science Letters*, *309*(3–4), 185–197. <https://doi.org/10.1016/j.epsl.2011.06.023>

Ishii, T., Kojitani, H., & Akaogi, M. (2019). Phase relations of Harzburgite and MORB up to the uppermost lower mantle conditions: Precise comparison with Pyrolite by multisample cell high-pressure experiments with implication to dynamics of subducted slabs. *Journal of Geophysical Research: Solid Earth*, *124*, 3491–3507. <https://doi.org/10.1029/2018JB016749>

Ishii, T., Liu, Z., & Katsura, T. (2019). A breakthrough in pressure generation by a Kawai-type multi-anvil apparatus with tungsten carbide anvils. *Engineering*, *5*(3), 434–440. <https://doi.org/10.1016/j.eng.2019.01.013>

- Kang, K., Koh, Y. K., Chiritescu, C., Zheng, X., & Cahill, D. G. (2008). Two-tint pump-probe measurements using a femtosecond laser oscillator and sharp-edged optical filters. *Review of Scientific Instruments*, 79(11), 114901. <https://doi.org/10.1063/1.3020759>
- Karato, S. I. (2011). Water distribution across the mantle transition zone and its implications for global material circulation. *Earth and Planetary Science Letters*, 301(3–4), 413–423. <https://doi.org/10.1016/j.epsl.2010.11.038>
- Karato, S. I., & Jung, H. (1998). Water, partial melting and the origin of the seismic low velocity and high attenuation zone in the upper mantle. *Earth and Planetary Science Letters*, 157(3–4), 193–207. [https://doi.org/10.1016/S0012-821X\(98\)00034-X](https://doi.org/10.1016/S0012-821X(98)00034-X)
- Khan, A., & Shankland, T. J. (2012). A geophysical perspective on mantle water content and melting: Inverting electromagnetic sounding data using laboratory-based electrical conductivity profiles. *Earth and Planetary Science Letters*, 317–318, 27–43. <https://doi.org/10.1016/j.epsl.2011.11.031>
- Kohlstedt, D. L., Keppeler, H., & Rubie, D. C. (1996). Solubility of water in the α , β and γ phases of $(\text{Mg, Fe})_2\text{SiO}_4$. *Contributions to Mineralogy and Petrology*, 123(4), 345–357. <https://doi.org/10.1007/s004100050161>
- Koyama, T., Shimizu, H., Utada, H., Ichiki, M., Ohtani, E., & Hae, R. (2006). Water content in the mantle transition zone beneath the North Pacific derived from the electrical conductivity anomaly. *Geophysical Monograph-American Geophysical Union*, 168, 171. <https://doi.org/10.1029/168GM13>
- Liang, X. (2017). Impact of grain boundary characteristics on lattice thermal conductivity: A kinetic theory study on ZnO. *Physical Review B*, 95(15), 155313. <https://doi.org/10.1103/PhysRevB.95.155313>
- Litasov, K., Ohtani, E., Langenhorst, F., Yurimoto, H., Kubo, T., & Kondo, T. (2003). Water solubility in Mg-perovskites and water storage capacity in the lower mantle. *Earth and Planetary Science Letters*, 211(1–2), 189–203. [https://doi.org/10.1016/S0012-821X\(03\)00200-0](https://doi.org/10.1016/S0012-821X(03)00200-0)
- Litasov, K., Ohtani, E., Sano, A., Suzuki, A., & Funakoshi, K. (2005). In situ X-ray diffraction study of post-spinel transformation in a peridotite mantle: Implication for the 660-km discontinuity. *Earth and Planetary Science Letters*, 238(3–4), 311–328. <https://doi.org/10.1016/j.epsl.2005.08.001>
- Litasov, K. D., Ohtani, E., & Sano, A. (2006). Influence of water on major phase transitions in the Earth's mantle. *Geophysical Monograph-American Geophysical Union*, 168, 95. <https://doi.org/10.1029/168GM08>
- Mao, H. K., Xu, J. A., & Bell, P. M. (1986). Calibration of the ruby pressure gauge to 800 kbar under quasi-hydrostatic conditions. *Journal of Geophysical Research*, 91(B5), 4673–4676. <https://doi.org/10.1029/JB091iB05p04673>
- McCammon, C. A., Frost, D. J., Smyth, J. R., Laustsen, H. M. S., Kawamoto, T., Ross, N. L., & Van Aken, P. A. (2004). Oxidation state of iron in hydrous mantle phases: Implications for subduction and mantle oxygen fugacity. *Physics of the Earth and Planetary Interiors*, 143–144, 157–169. <https://doi.org/10.1016/j.pepi.2003.08.009>
- Mei, S., & Kohlstedt, D. L. (2000). Influence of water on plastic deformation of olivine aggregates 1. Diffusion creep regime. *Journal of Geophysical Research*, 105(B9), 21,457–21,469. <https://doi.org/10.1029/2000JB900179>
- O'Hara, K. E., Hu, X., & Cahill, D. G. (2001). Characterization of nanostructured metal films by picosecond acoustics and interferometry. *Journal of Applied Physics*, 90(9), 4852–4858. <https://doi.org/10.1063/1.1406543>
- Ohtani, E. (2019). The role of water in Earth's mantle. *National Science Review*, 7(1), 224–232. <https://doi.org/10.1093/nsr/nwz071>
- Ohtani, E., Litasov, K., Hosoya, T., Kubo, T., & Kondo, T. (2004). Water transport into the deep mantle and formation of a hydrous transition zone. *Physics of the Earth and Planetary Interiors*, 143–144, 255–269. <https://doi.org/10.1016/j.pepi.2003.09.015>
- Ohtani, E., Mizobata, H., & Yurimoto, H. (2000). Stability of dense hydrous magnesium silicate phases in the systems $\text{Mg}_2\text{SiO}_4\text{-H}_2\text{O}$ and $\text{MgSiO}_3\text{-H}_2\text{O}$ at pressures up to 27 GPa. *Physics and Chemistry of Minerals*, 27(8), 533–544. <https://doi.org/10.1007/s002690000097>
- Panero, W. R., Smyth, J. R., Pigott, J. S., Liu, Z., & Frost, D. J. (2013). Hydrous ringwoodite to 5 K and 35 GPa: Multiple hydrogen bonding sites resolved with FTIR spectroscopy. *American Mineralogist*, 98(4), 637–642. <https://doi.org/10.2138/am.2013.3978>
- Pearson, D. G., Brenker, F. E., Nestola, F., McNeill, J., Nasdala, L., Hutchison, M. T., et al. (2014). Hydrous mantle transition zone indicated by ringwoodite included within diamond. *Nature*, 507(7491), 221–224. <https://doi.org/10.1038/nature13080>
- Ranero, C. R., Morgan, J. P., McIntosh, K., & Reichert, C. (2003). Bending-related faulting and mantle serpentinization at the Middle America trench. *Nature*, 425(6956), 367–373. <https://doi.org/10.1038/nature01961>
- Richard, G., Bercovici, D., & Karato, S. I. (2006). Slab dehydration in the Earth's mantle transition zone. *Earth and Planetary Science Letters*, 251(1–2), 156–167. <https://doi.org/10.1016/j.epsl.2006.09.006>
- Rüpke, L. H., Phipps Morgan, J., Hort, M., & Connolly, J. A. D. (2004). Serpentine and the subduction zone water cycle. *Earth and Planetary Science Letters*, 223(1–2), 17–34. <https://doi.org/10.1016/j.epsl.2004.04.018>
- Saxena, S. K. (1996). Earth mineralogical model: Gibbs free energy minimization computation in the system $\text{MgO} \text{---} \text{FeO} \text{---} \text{SiO}_2$. *Geochimica et Cosmochimica Acta*, 60(13), 2379–2395. [https://doi.org/10.1016/0016-7037\(96\)00096-8](https://doi.org/10.1016/0016-7037(96)00096-8)
- Schmandt, B., Jacobsen, S. D., Becker, T. W., Liu, Z., & Dueker, K. G. (2014). Dehydration melting at the top of the lower mantle. *Science*, 344(6189), 1265–1268. <https://doi.org/10.1126/science.1253358>
- Schmidt, A., Chiesa, M., Chen, X., & Chen, G. (2008). An optical pump-probe technique for measuring the thermal conductivity of liquids. *Review of Scientific Instruments*, 79(6), 064902. <https://doi.org/10.1063/1.2937458>
- Schmidt, M. W., & Poli, S. (1998). Experimentally based water budgets for dehydrating slabs and consequences for arc magma generation. *Earth and Planetary Science Letters*, 163(1–4), 361–379. [https://doi.org/10.1016/S0012-821X\(98\)00142-3](https://doi.org/10.1016/S0012-821X(98)00142-3)
- Schulze, K., Marquardt, H., Kawazoe, T., Ballaran, T. B., McCammon, C., Koch-Müller, M., et al. (2018). Seismically invisible water in Earth's transition zone? *Earth and Planetary Science Letters*, 498, 9–16. <https://doi.org/10.1016/j.epsl.2018.06.021>
- Su, C., Liu, Y., Song, W., Fan, D., Wang, Z., & Tang, H. (2018). Thermodynamic properties of San Carlos olivine at high temperature and high pressure. *Acta Geochimica*, 37(2), 171–179. <https://doi.org/10.1007/s11631-018-0261-z>
- Suetsugu, D., Inoue, T., Obayashi, M., Yamada, A., Shiobara, H., Sugioka, H., et al. (2010). Depths of the 410-km and 660-km discontinuities in and around the stagnant slab beneath the Philippine Sea: Is water stored in the stagnant slab? *Physics of the Earth and Planetary Interiors*, 183(1–2), 270–279. <https://doi.org/10.1016/j.pepi.2010.09.004>
- Suzuki, A., Ohtani, E., Morishima, H., Kubo, T., Kanbe, Y., Kondo, T., et al. (2000). In situ determination of the phase boundary between wadsleyite and ringwoodite in Mg_2SiO_4 . *Geophysical Research Letters*, 27(6), 803–806. <https://doi.org/10.1029/1999GL008425>
- Syracuse, E. M., van Keken, P. E., & Abers, G. A. (2010). The global range of subduction zone thermal models. *Physics of the Earth and Planetary Interiors*, 183(1–2), 73–90. <https://doi.org/10.1016/j.pepi.2010.02.004>
- Thomas, S. M., Bina, C. R., Jacobsen, S. D., & Goncharov, A. F. (2012). Radiative heat transfer in a hydrous mantle transition zone. *Earth and Planetary Science Letters*, 357–358, 130–136. <https://doi.org/10.1016/j.epsl.2012.09.035>
- Thomas, S.-M., Jacobsen, S. D., Bina, C. R., Reichart, P., Moser, M., Hauri, E. H., et al. (2015). Quantification of water in hydrous ringwoodite. *Frontiers in Earth Science*, 2, 38. <https://doi.org/10.3389/feart.2014.00038>
- Tschauner, O., Huang, S., Greenberg, E., Prakapenka, V. B., Ma, C., Rossman, G. R., et al. (2018). Ice-VII inclusions in diamonds: Evidence for aqueous fluid in Earth's deep mantle. *Science*, 359(6380), 1136–1139. <https://doi.org/10.1126/science.aao3030>

- Turcotte, D. L., & Schubert, G. (2014). *Geodynamics*, (p. 636). Cambridge: Cambridge University Press. <https://doi.org/10.1017/CBO9780511843877>
- Utada, H., Koyama, T., Obayashi, M., & Fukao, Y. (2009). A joint interpretation of electromagnetic and seismic tomography models suggests the mantle transition zone below Europe is dry. *Earth and Planetary Science Letters*, *281*(3–4), 249–257. <https://doi.org/10.1016/j.epsl.2009.02.027>
- Van Der Meer, D. G., Spakman, W., Van Hinsbergen, D. J., Amaru, M. L., & Torsvik, T. H. (2010). Towards absolute plate motions constrained by lower-mantle slab remnants. *Nature Geoscience*, *3*(1), 36–40. <https://doi.org/10.1038/ngeo708>
- van Keken, P. E., Hacker, B. R., Syracuse, E. M., & Abers, G. A. (2011). Subduction factory: 4. Depth-dependent flux of H₂O from subducting slabs worldwide. *Journal of Geophysical Research*, *116*, B01401. <https://doi.org/10.1029/2010JB007922>
- Xu, Y., Shankland, T. J., Linhardt, S., Rubie, D. C., Langenhorst, F., & Klasinski, K. (2004). Thermal diffusivity and conductivity of olivine, wadsleyite and ringwoodite to 20 GPa and 1373 K. *Physics of the Earth and Planetary Interiors*, *143–144*, 321–336. <https://doi.org/10.1016/j.pepi.2004.03.005>
- Ye, Y., Brown, D. A., Smyth, J. R., Panero, W. R., Jacobsen, S. D., Chang, Y. Y., et al. (2012). Compressibility and thermal expansion of hydrous ringwoodite with 2.5 (3) wt% H₂O. *American Mineralogist*, *331–332*(4), 112–119. <https://doi.org/10.1016/j.epsl.2012.03.001>
- Yoshino, T., Manthilake, G., Matsuzaki, T., & Katsura, T. (2008). Dry mantle transition zone inferred from the conductivity of wadsleyite and ringwoodite. *Nature*, *451*(7176), 326–329. <https://doi.org/10.1038/nature06427>
- Zhang, J. S., & Bass, J. D. (2016). Sound velocities of olivine at high pressures and temperatures and the composition of Earth's upper mantle. *Geophysical Research Letters*, *43*, 9611–9618. <https://doi.org/10.1002/2016GL069949>
- Zhang, Y., Yoshino, T., Yoneda, A., & Osako, M. (2019). Effect of iron content on thermal conductivity of olivine with implications for cooling history of rocky planets. *Earth and Planetary Science Letters*, *519*, 109–119. <https://doi.org/10.1016/j.epsl.2019.04.048>
- Zhao, D. (2004). Global tomographic images of mantle plumes and subducting slabs: Insight into deep Earth dynamics. *Physics of the Earth and Planetary Interiors*, *146*(1–2), 3–34. <https://doi.org/10.1016/j.pepi.2003.07.032>
- Zheng, X., Cahill, D. G., Krasnochtchekov, P., Averback, R. S., & Zhao, J. C. (2007). High-throughput thermal conductivity measurements of nickel solid solutions and the applicability of the Wiedemann–Franz law. *Acta Materialia*, *55*(15), 5177–5185. <https://doi.org/10.1016/j.actamat.2007.05.037>